# The quantum nature of the OH stretching mode in ice and water probed by neutron scattering experiments

Roberto Senesi, Davide Flammini, Alexander I. Kolesnikov, Éamonn D. Murray, Giulia Galli, and Carla Andreani

Citation: The Journal of Chemical Physics **139**, 074504 (2013); doi: 10.1063/1.4818494
View online: http://dx.doi.org/10.1063/1.4818494
View Table of Contents: http://scitation.aip.org/content/aip/journal/jcp/139/7?ver=pdfcov
Published by the AIP Publishing

# The quantum nature of the OH stretching mode in ice and water probed by neutron scattering experiments

Roberto Senesi,[1,2,a)] Davide Flammini,[1] Alexander I. Kolesnikov,[3] Éamonn D. Murray,[4] Giulia Galli,[4] and Carla Andreani[1]
[1]*Dipartimento di Fisica e Centro NAST, Università degli Studi di Roma "Tor Vergata," Via della Ricerca Scientifica 1, 00133 Roma, Italy*
[2]*Consiglio Nazionale delle Ricerche, CNR-IPCF, Sezione di Messina, Italy*
[3]*Neutron Scattering Science Division, Oak Ridge National Laboratory, Tennessee 37831-6460, USA*
[4]*University of California, Davis, California 95616, USA*

(Received 17 May 2013; accepted 1 August 2013; published online 21 August 2013)

The OH stretching vibrational spectrum of water was measured in a wide range of temperatures across the triple point, 269 K $< T <$ 296 K, using Inelastic Neutron Scattering (INS). The hydrogen projected density of states and the proton mean kinetic energy, $\langle E_K \rangle_{OH}$, were determined for the first time within the framework of a harmonic description of the proton dynamics. We found that in the liquid the value of $\langle E_K \rangle_{OH}$ is nearly constant as a function of T, indicating that quantum effects on the OH stretching frequency are weakly dependent on temperature. In the case of ice, *ab initio* electronic structure calculations, using non-local van der Waals functionals, provided $\langle E_K \rangle_{OH}$ values in agreement with INS experiments. We also found that the ratio of the stretching ($\langle E_K \rangle_{OH}$) to the total ($\langle E_K \rangle_{exp}$) kinetic energy, obtained from the present measurements, increases in going from ice, where hydrogen bonding is the strongest, to the liquid at ambient conditions and then to the vapour phase, where hydrogen bonding is the weakest. The same ratio was also derived from the combination of previous deep inelastic neutron scattering data, which does not rely upon the harmonic approximation, and the present measurements. We found that the ratio of stretching to the total kinetic energy shows a minimum in the metastable liquid phase. This finding suggests that the strength of intermolecular interactions increases in the supercooled phase, with respect to that in ice, contrary to the accepted view that supercooled water exhibits weaker hydrogen bonding than ice. © *2013 AIP Publishing LLC*. [http://dx.doi.org/10.1063/1.4818494]

## I. INTRODUCTION

Water continues to be the focus of many experimental and theoretical investigations, given its relevance to numerous fields of science.[1–3] One of the outstanding questions regarding water and ice is the influence of the quantum nature of hydrogen atoms on their physical and chemical properties, as a function of temperature (T). In recent years, several Deep Inelastic Neutron Scattering (DINS) experiments and theoretical studies were performed to elucidate the proton quantum state, e.g., by investigating the proton momentum distribution, $n(p)$ and the mean proton kinetic energy $\langle E_K \rangle$. The momentum distribution provides direct information about the effective potential acting upon the protons; the value of $\langle E_K \rangle$, being essentially determined by zero point motion, allows one to quantify nuclear quantum effects.[4,5] In particular, if one decomposes the motion of the protons into stretching, bending, librational and translational components,[6] $\langle E_K \rangle$ may be approximated by the sum of vibrational contributions, the most prominent component being that of the stretching mode.

Recently, the momentum distribution of water and ice was probed experimentally using neutrons of eV energy and by measuring the proton dynamics on an attosecond time scale,[7–12] using DINS. Currently, this technique is available only at the VESUVIO beam line operating at the ISIS neutron facility.[13–15] Measurements were carried out on ice and liquid water, in stable and metastable phases, in a wide temperature range, 269 K $< T <$ 673 K. Experimental results showed a remarkably diverse behavior of the mean proton kinetic energy $\langle E_K \rangle$ and of $n(p)$ as a function of T.[4,11,12,16–18] While a quantitative agreement between experiments and theoretical predictions, using independent DINS data analyses, was found for the proton momentum distributions in ice[18] and supercritical water,[19] discrepancies were reported for liquid water at room temperatures and below. Of particular significance is the excess of $\langle E_K \rangle$ observed across the density maximum at 277 K and across the supercooled phase at 272 K,[16] whose interpretation is still the subject of debate.

Several computer simulations of momentum distributions in water and ice were also pursued; these studies used empirical flexible and polarizable models,[20] open Path Integral Molecular Dynamics and open Path Integral Car-Parrinello Molecular Dynamics (PICPMD) performed on high pressure phases of ice.[21,22] It is now well established that the stronger the O–H covalent bond, the larger the proton momentum width.[19,20] Indeed, the tail of the distribution is due to the momentum along the bond direction, since the proton is most tightly bound in this direction, and tight binding implies high momentum width. Hence, the high-momentum tail of the

a)Electronic mail: roberto.senesi@uniroma2.it

 

$n(p)$ line shape provides information about the strength and anharmonicity of the O–H stretching mode, as discussed, e.g., in Refs. 20 and 23 and Figure 3 of Ref. 19. Upon increasing the hydrogen bond (H-bond) strength, the effective proton potential softens and consequently the $\langle E_K \rangle$ and the O–H stretching frequency decreases (i.e., the O–H stretching frequency red shifts as the H-bond strength increases).[20–22,24–26]

The redshift of the intramolecular stretching frequency of ice vibrational spectra, as compared to water and supercooled water (SW) spectra, is generally interpreted as a fingerprint of stronger H-bonding in ice.[27–30] In a recent study,[31] however, the redshift of the intramolecular stretching frequency was also proposed as a descriptor that could be used to estimate the interplay between quantum effects arising from zero point motion, and the strength of H- bonds, for a variety of systems ranging from $H_2O$ clusters, and HF dimers to solid HF and squaric acid. In particular, it has been suggested that nuclear quantum effects tend to weaken weak H-bonds and to strengthen strong ones, showing that this correlation holds for a large variety of H-bonded systems. The mechanism invoked is a competition between anharmonic quantum fluctuations of intermolecular H-bond bending – which tends to weaken H-bonds – and intramolecular covalent bond stretching (elongation) – which tends to strengthen H-bonds. Indeed, in the study of water clusters presented in Ref. 31, it was shown that quantum simulations yield O–O distances, which characterize the intermolecular separations, longer than those found in classical simulations; this was correlated with the calculated values of the projection of donor O–H bond length along the intermolecular axis: the quantum-calculated values for water were shorter than those found in classical simulations. Thus, nuclear quantum effects were found to weaken H-bonding in water.[31] On the other hand, in systems such as large HF clusters, up to the pentamer, quantum simulations in Ref. 31 showed an opposite trend, i.e., nuclear quantum effects cause a reduction of F–F distances, an elongation of the F–H bond length, a reduction of the intermolecular H-bond bending, and a marked redshift of the stretching frequency, leading to an overall strengthening of H-bonding due to quantum effects.

Supercooled water may represent an exception to the trend identified in Ref. 31: neutron diffraction measurements on supercooled water at 270 K[32,33] indicate that the first and second peaks of the O–O radial distributions are at a shorter distance than in ambient water, e.g., the distance of the first O–O peak maximum shortens from about 2.76 Å, for ambient water, to 2.70 Å in supercooled water; the same shift is observed between ice and supercooled water: the O–O maximum in ice at 220 K is at 2.79 Å[34,35] (with a mean distance of 2.75 Å as determined from extended x-ray absorption fine structure experiments at T = 256 K[36]), compared to 2.70 Å in supercooled water.[32,33] The second O–O peak distance shortens from about 4.60 Å, in ambient water, to 4.30 Å in supercooled water.[32,33] Moreover, Refs. 32, 33 report a marked sharpening of the bi-modal character of the distribution of $O\hat{O}O$ angles with respect to that of ambient water, corresponding to both increased tetrahedral coordination and an increased presence of "interstitial" molecules, i.e., molecules "not directly H-bonded to the central one."[32,33] These findings indicate the simultaneous occurrence, upon supercooling, of a reduced heavy atom intermolecular distance (increased H-bonding) and a substantial H-bond bending (decreased H-bonding), which deserve to be better probed by studies of the single-particle dynamics on short (down to the attosecond range) timescales by techniques such as DINS and INS.[1,10,12,18]

In this work, we determined the mean kinetic energy $\langle E_K \rangle_{OH}$ of the OH stretching mode for the first time, and we used the ratio $\frac{\langle E_K \rangle_{OH}}{\langle E_K \rangle}$ to characterize the strength of H-bonding in water as a function of temperature, in a range including ice, the stable and the metastable liquid. We derived the density of states (DOS), $g_{exp}(E)_{OH}$, the momentum distribution, $n_{OH}(p)$, and mean kinetic energy, $\langle E_K \rangle_{OH}$ from neutron scattering measurements (INS and previously published DINS measurements), and we used the results of electronic structure calculations with van der Waals functionals to interpret some of our experiments. We analyzed the data obtained by INS measurements using the harmonic approximation:[29,37,38] from the vibrational spectra we obtained the hydrogen projected density of states and momentum distribution, $g_{exp}(\mathrm{E})_H$ and $n_H(p)$, respectively. From the OH stretching component of the H-projected density of states, $g_{exp}(\mathrm{E})_{OH}$, we then derived $\langle E_K \rangle_{OH}$ (T) and $n_{OH}(p)$. The analyses of these quantities allowed us to understand how the quantum nature of protons affects the OH stretching mode of stable, supercooled water and of ice as a function of T.[21,22,24–26] Furthermore, we used a combined analysis of theoretical and experimental line shapes to separate the harmonic and anharmonic components of the proton momentum distribution, $n_H(p)$, as well as its intramolecular stretching component, $n_{OH}(p)$.

The rest of the paper is organized as follows: In Sec. II, we describe the methods and techniques used in our study, in Sec. III we present our results, and our conclusions are given in Sec. IV.

## II. EXPERIMENTAL TECHNIQUES AND THEORETICAL METHODS

Within the harmonic approximation,[29] $g_{exp}(\mathrm{E})_H$ is directly proportional to the one-phonon incoherent dynamical structure factor, $S_{inc}(q, E)$, with $E = \hbar\omega$ being the energy transfer in the scattering process. The quantity $q = k_i - k_f$ is the wavevector transfer, with $k_f$ and $k_i$ being the final and incident neutron wavevectors, respectively. For hydrogenous polycrystalline or isotropic materials, $S_{inc}(q, E)$ is given by

$$S_{inc}(q, E) = \frac{N}{2M} q^2 \frac{g_{exp}(E)_H}{E} [n(E) + 1] e^{[-2W(q)]}, \qquad (1)$$

where M is the proton mass, $n(E)$ is the Bose population factor,[38] and the experimental data are normalized to the number $N$ of scattering centers. The main vibrational bands in a $S_{inc}(q, E)$ spectrum are composed of a stretching band centered at ≈417 meV, a bending band centered at ≈200 meV, a broad libration band centered at ≈80 meV. The $e^{[-2W(q)]}$ is the Debye Waller factor (DWF), which for an isotropic harmonic potential is given by $e^{[-q^2\langle u^2 \rangle]}$, where $\langle u^2 \rangle$ is the proton mean

squared displacement. Thus, $g_{exp}(E)_H$ can be derived by the $S_{inc}(q, E)$ by simply performing an extrapolation to $q \rightarrow 0$, at constant $\hbar\omega$, of the ratio $S_{inc}(q, E)/q^2$

$$lim_{q\rightarrow 0}\frac{S_{inc}(q, E)}{q^2}2ME\frac{e^{[2W(q)]}}{[n(E)+1]} = g_{exp}(E)_H. \quad (2)$$

It was shown that this procedure is reliable if $S_{inc}(q, E)$ data are collected in a wide range of $q$ and for $q$ values as low as possible; this will ensure the ratio $S_{inc}(q, E)e^{[2W(q)]}/q^2$ has a linear behavior for all the constant E values for which the $q \rightarrow 0$ extrapolation is performed (see Figure 5 in Ref. 38).

The experimental H-projected density of states, $g_{exp}(E)_H$, and its OH stretching vibrational mode component, $g_{exp}(E)_{OH}$, were derived using Eq. (2). The simulated H projected density of states, $g_{sim}(E)_H$, was obtained through density functional theory (DFT) calculations,[39] with the vdW-DF2[40] approximation to exchange-correlation which includes dispersion interactions. These calculations were carried out on the ice XI phase as described in Ref. 24, and the H projected density of states was obtained via the eigenvectors of the dynamical matrix.

In the following, we give details of techniques and our *ab initio* calculations.

### A. Neutron scattering experiment

INS at high incident energies and low momentum transfer is a powerful technique to determine the vibrational spectra of H-bonded systems. For example, the anomalous soft dynamics of water in nanotubes has been unraveled using INS,[41] which showed a flat-bottom proton potential. In the present study, INS was used to collect unique information on water using the H-projected vibrational density of states in the energy range of the OH stretching modes. In principle, this piece of information can also be obtained from the IR and Raman spectroscopies. However, in the case of water and ice, the selection rules governing the interaction of light radiation with matter in perfectly ordered systems do not apply due to the local structure disorder (or proton disorder in the case of ice). This makes the analysis of the spectral IR and Raman intensities much more complex than in crystalline solids. Rather comprehensive, quantitative, and more direct information on the vibrational spectrum can instead be obtained by INS where one measures the dynamical structure factor which is directly related to the density of vibrational states, weighted by the squared amplitudes of the atomic oscillations.[29,37,38] Hence, using INS one can measure not only translational, librational, and intra-molecular excitations energies but also spectral intensities.

The INS experiments were carried out on water in the range 269 K $< T <$ 296 K, using the time-of-flight neutron chopper spectrometer SEQUOIA at the SNS.[42] A high neutron incident energy, $E_i = 600$ meV, was chosen in order to minimize the momentum transfer at small scattering angles, thus reducing the effect of the Debye-Waller factor and neutron multiphonon scattering. At this $E_i$, the spectrometer energy resolution was high enough to resolve the shift in the position of intermolecular and intramolecular modes due to the change of water proton effective potential.[43] The sample container was a flat aluminum holder, with a 50 × 50 mm$^2$ cross-section and an internal thickness of 0.25 mm. The inner surface was Teflon coated to prevent ice nucleation. The container was located perpendicular to the incident neutron beam. In the supercooled phase, special care was taken to monitor for the occurrence of ice formation by recording both the latent heat of solidification released by the temperature controls and the spectral features associated with ice formation in the INS spectra. A total of 14 INS spectra were recorded in ice at T = 271 K, in the SW metastable phase at T = 269 K, T = 271 K, and in the water stable phase at T = 273 K, T = 274 K, T = 275 K, T = 276 K, T = 277 K, T = 278 K, T = 280 K, T = 281 K, T = 285 K, T = 290 K, and T = 296 K (see Table II). The INS measurements were performed for a sample in the container, the empty container, the background, and a vanadium plate of the same sample geometry. The background from the empty container was subtracted from the raw data, and the vanadium run provided data for detector calibration and intensity normalization of the spectra. Data were recorded using $^3$He neutron detectors, covering a scattering angular range $4^\circ < 2\theta < 56^\circ$, with an angular increment of 0.26°. The collected INS data were transformed from the time-of-flight and instrument coordinates to the dynamical structure factor, $S_{exp}(2\theta, E)$, in an energy range – 200 meV $< E <$ 550 meV, with an energy bin of 2 meV and with angular increment of 2°. The data treatment also included the corrections for the efficiency of $^3$He neutron detectors as a function of energy and for the kinematical factor $k_f/k_i$.

### B. Data analysis

At each temperature, individual $S_{exp}(2\theta, E)$ spectra, as a function of $E$, were extracted for all $\theta$ values, using standard analysis software available on SEQUOIA. Figure 1, central panel, reports the intensity of $S_{exp}(2\theta, E)$ spectra at $2\theta = 12^\circ$ scattering angle, as a function of energy transfer for ice at T = 271 K and supercooled water at T = 271 K and water at T = 296 K. These plots show clearly the distinct features of the vibrational spectrum of ice in the whole range of energy transfers, as compared to both water and supercooled water at different temperatures. Similar distinct features in the vibrational spectra of ice and stable and metastable water are observed at all the other investigated temperatures (see, for example, top panel of Figure 1). The more remarkable feature is the red-shift of the ice OH stretching band as compared to the same band in water and supercooled water (see Figure 1, top panel). In order to derive the $S_{inc}(q, E)$, one still needs to correct each experimental spectra at each scattering angle for the multiple scattering (MS) contribution.

The latter was evaluated using a phenomenological approach which relies on the use of the Impulse Approximation (IA),[13] originally proposed in an INS experiment on ice.[29] This approach was shown to be quantitatively reliable in several previous INS measurements from hydrogenous samples contained in a slab-geometry used in conjunction with direct geometry spectrometers, such as SEQUOIA.[29,37,38] The probabilities of MS events are dependent on the thickness of the sample: for a slab geometry container with thickness

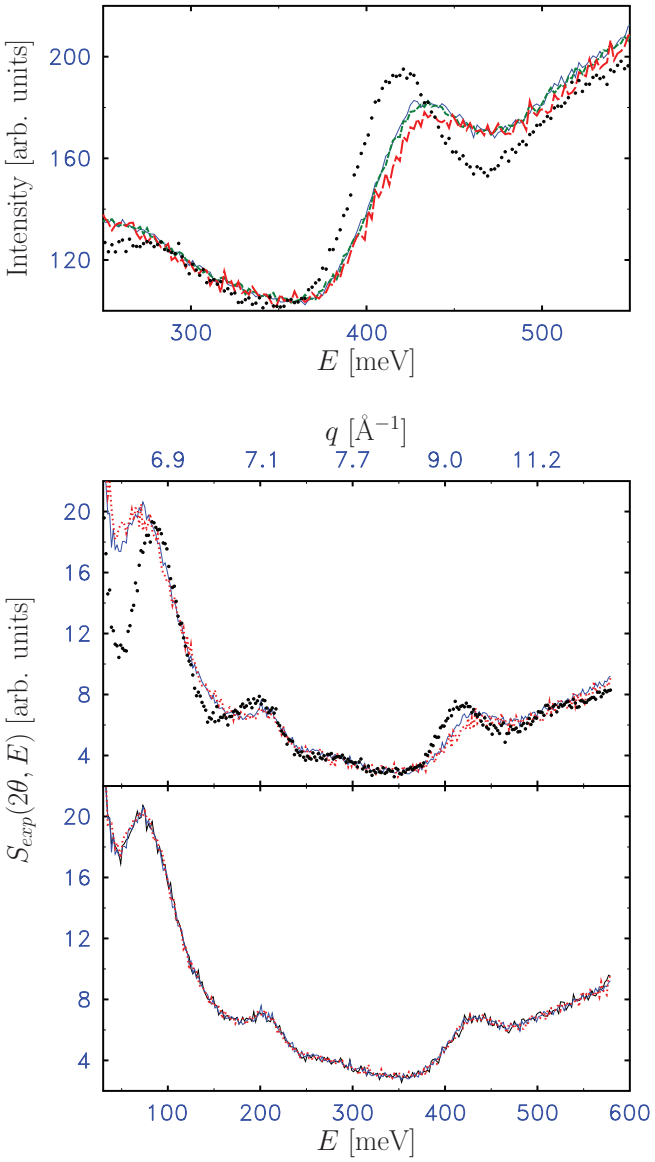


FIG. 1. (Top panel) Sum of $S_{exp}(2\theta, E)$ experimental INS spectra between $4^\circ < 2\theta < 54^\circ$, for ice (black dots), water, at T = 276 K (green dashed line) and at T = 296 K (red dashed-dotted line), supercooled water at T = 271 K (blue continuous line), around the stretching peak. (Central panel) $S_{exp}(2\theta, E)$ spectra, for $2\theta = 12^\circ$ scattering angle, as a function of energy transfer for ice at T = 271 K (black dots), supercooled water at T = 271 K (blue line) and water at T = 296 K (red dots). The peak associated with O–H stretching in ice is visible at E = 417 meV. (Bottom panel) $S_{exp}(2\theta, E)$ spectra, for $2\theta = 12^\circ$ scattering angle, as a function of energy transfer for supercooled water at T = 271 K (blue line), water at T = 273 K (black line), and T = 276 K (red dashed line); the peak associated with O–H stretching is at 430 meV.

$d$ and lateral dimension $L$, the MS contribution is expected to be relevant at low angles. However, in the limiting case of $L \gg d$, most of the MS at low scattering angles is due to two single scattering events 90° or ≃90° apart. It can be shown that these events make up the majority of the MS contribution[37] with a total contribution of about 6% , as estimated using the Sears formula.[44] Within the IA for neutron scattering at high incident energy, such as $E = 600$ meV, each single scattering event can be modeled by a Gaussian function, $G(q, E) = Ae^{-[E-E_R]^2/(2\sigma_0^2)}$, centered at the recoil energy $E_R = \hbar^2 q^2/2M$, with $\sigma_0$ as a free parameter. The convolution of two $G(q, E)$ provides the MS contribution to experimental $S(q, E)$, which can be expressed as $A'e^{-[E-2E_R]^2/(2\sigma^2)}$ where $\sigma^2 = 2\sigma_0^2$. The absolute intensity factor $A$ was derived by normalizing each $S_{inc}(q, E)$ at all $2\theta$ values bearing in mind the ratio between the intensities of double and single scattering obtained by the Sears' formula.[44] We stress that this phenomenological approach, i.e., multiple scattering modeled by double events within the IA, applies only above approximately 200 meV.[37]

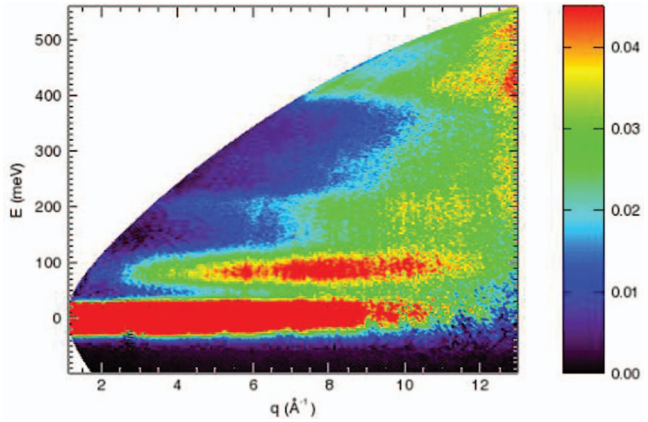


FIG. 2. The $(q, E)$ contour plot for the intensity of $S(q, E)$ data for ice at T = 271 K, measured with an incident neutron energy $E_i = 600$ meV.

Examples of contour plots, showing the map of the full kinematic range of the present measurements, of the $S_{exp}(2\theta, E)$ data obtained in the $(q, E)$ plane for ice and supercooled water at T = 271 K are reported in Figures 2 and 3, respectively.

The incoherent dynamical structure factors $S_{inc}(q, E)$, obtained after correcting for the MS contribution for all T, at a scattering angle $2\theta = 12^\circ$, are plotted in Figure 4. These functions are all normalized to unit area, according to the first moment sum rule.[29]

For the data in the range $4^\circ < 2\theta < 20^\circ$, using the $S_{inc}(q, E)$ normalized to 1, the H- projected density of states $g_{exp}(E)_H$ can be extracted at each experimental T, using Eq. (2) as follows. For example, for the OH stretching band

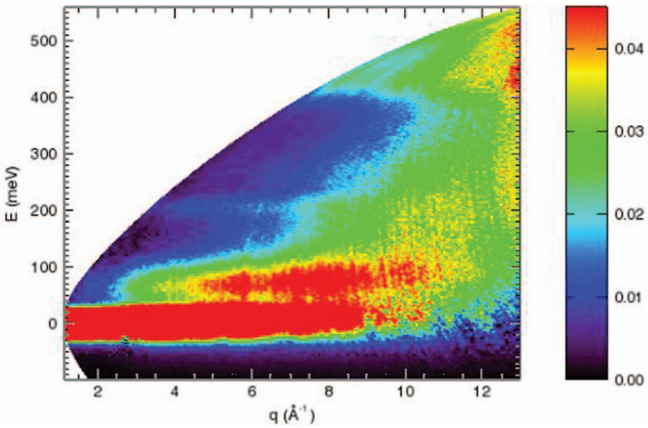


FIG. 3. The $(q, E)$ contour plot for the intensity of $S(q, E)$ data for supercooled water at T = 271 K, measured with an incident neutron energy $E_i = 600$ meV.

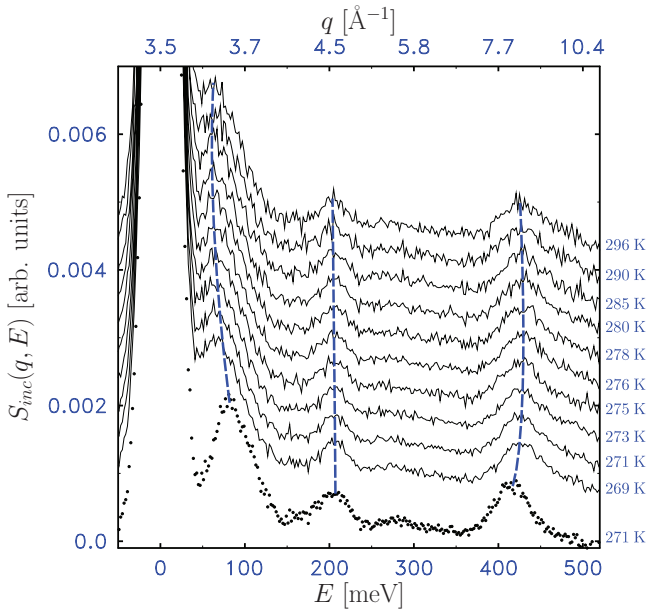


FIG. 4. The function $S_{inc}(q, E)$ (defined in Eq. (1)) corrected for multiple scattering at $2\theta = 12^\circ$ scattering angle. The data are presented as a function of temperature, from ice (bottom, solid circles) through supercooled water to water (continuous lines); the blue dashed lines mark the temperature dependence of the vibrational bands and are intended as a guide to the eye.

$\lim_{q\to 0} \Gamma(q, E) = \lim_{q\to 0} \frac{S_{inc}(q,E)}{q^2} k = g_{exp}(E)_{OH}$, where

$$\Gamma(q, E) = g_{exp}(E)_{OH} + \alpha q^2. \quad (3)$$

Figure 5 reports examples of $\Gamma(q, E)$ versus $q^2$ plots for some selected E values in the region of OH stretching band. At each E, a best linear fit of the intensity as a function of $q^2$ is performed, such that the intercept at $lim_{q\to 0}$ provides the value

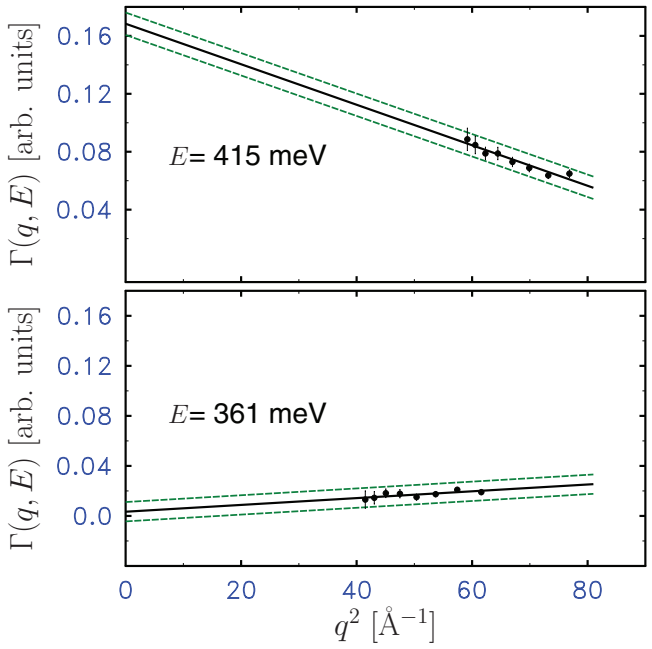


FIG. 5. The function $\Gamma(q, E)$ (defined in Eq. (3)) as a function of $q^2$ for two selected energy transfer of INS spectra, and their extrapolated values at $q = 0$ in the OH stretching band of ice at T = 271 K.

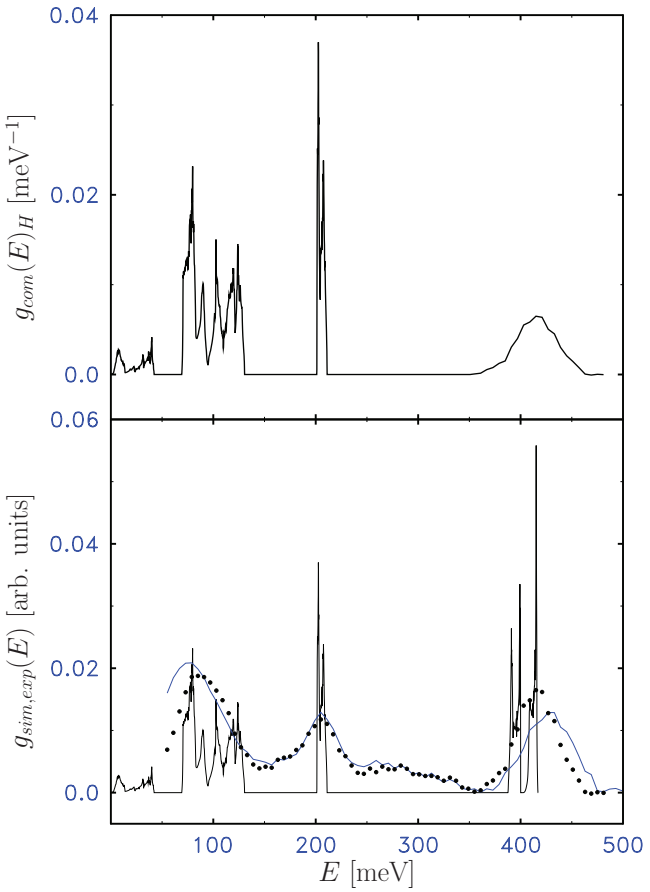


FIG. 6. (Top panel) The proton projected density of states for ice, $g_{com}(E)_H$, obtained by a suitable combination of $g_{exp}(E)_{OH}$ and $g_{sim}(E)_H$ (see Eqs. (5) and (6)). (Bottom panel) Experimental $g_{exp}(E)_H$ line shapes for supercooled water at T = 271 K (blue line) and for ice at T = 271 K (solid circles), compared with simulated full proton projected density of state, $g_{sim}(E)_H$, for ice at T = 0 K (black solid line). $g_{exp}(E)_H$ is not normalized.

for $g_{exp}(E)_{OH}$ at that energy. This fit is plotted with a black line in Figure 5, while green lines provide an estimate of the errors bar for $g_{exp}(E)_{OH}$. The Bose population factor in the present experiment is $\simeq 0$ and for the Debye-Waller factor a value of $\simeq 0.072$ Å$^2$ was used for the mean squared displacement of the hydrogen. Our results for $g_{exp}(E)_H$ and $g_{exp}(E)_{OH}$ functions are plotted in Figures 6 and 7, respectively.

### C. *Ab initio* calculations

In our analysis, we started from the results of density functional theory calculations presented in Ref. 24, where we used the QUANTUM ESPRESSO[39] code. The proton ordered ice XI structure was adopted as a model of proton disordered hexagonal ice, with the vdW-DF2[40] density functional used to include non-local correlation effects. Calculations were performed using a 4 × 4 × 4 k-point grid, and a plane wave energy cutoff of 160 Ry together with norm conserving pseudopotentials.[45] The phonon density of states was calculated on a 4 × 4 × 4 grid of wave vectors using density functional perturbation theory. Frequencies were obtained over a 12 × 12 × 12 grid using Fourier interpolation. The QUANTUM ESPRESSO phonon code was then modified to generate the

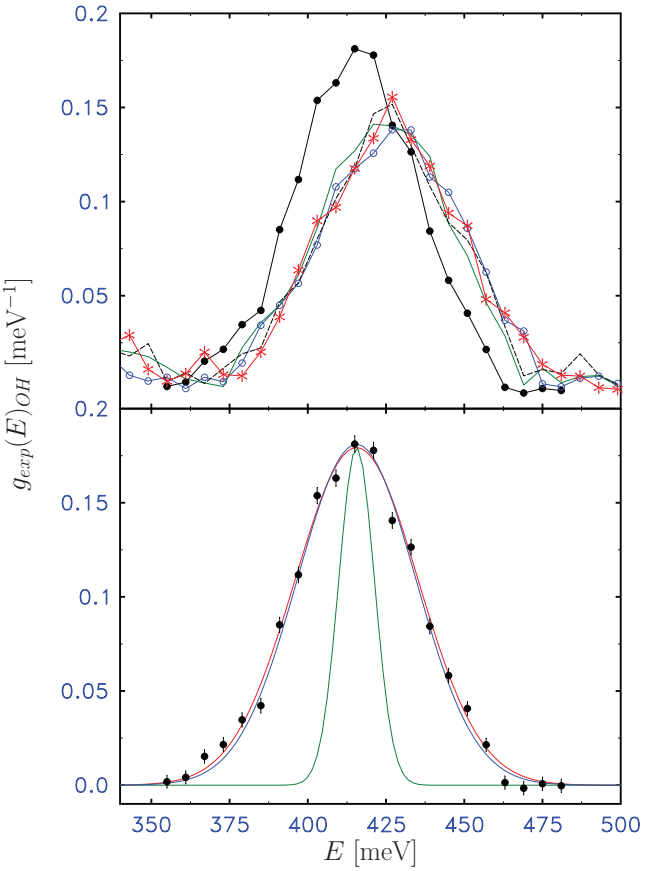


FIG. 7. (Top panel) The functional $g_{exp}(E)_{OH}$ (see Eq. (6)) for ice (solid circles, black line), supercooled water at T = 271 K (open circles, blue line) and water at T = 276 K (green continuous line), 278 K (black dashed line), 296 K (asterisks, red line). (Bottom panel) Fit of the $g_{exp}(E)_{OH}$ for ice (red line), the instrumental resolution function for SEQUOIA, $R(E)$ (green line), the $g_{exp}(E)_{OH}$ with the $R(E)$ function subtracted off (blue line).

hydrogen projected density of states via the phonon eigenvectors. The simulated hydrogen projected density of states, $g_{sim}(E)_H$, derived from density functional theory calculations for the ice data is reported in Figure 6. The calculations were also repeated with the Perdew-Burke-Ernzerhof (PBE) exchange correlation functional to estimate the effect of using a density functional without non-local correlation effects.

## III. RESULTS AND DISCUSSION

A comparison of the simulated $g_{sim}(E)$ at T = 0 K and two experimental $g_{exp}(E)$, derived from Eq. (2), for supercooled water at T = 271 K and ice at T = 271 K are plotted in the bottom panel of Figure 6. Figure 7 (bottom panel) shows the $g_{exp}(E)_{OH}$ for ice (full circle with error bars) and its Gaussian best fits, with (red line) and without (blue line) the instrument resolution function component, $R(E)$ (green line). The $R(E)$, which is almost constant and $q$ independent in the energy range of the present INS experiments, is well described by a Gaussian line shape with a FWHM (Full Width Half Maximum) of 12-14 meV. For the whole set of INS experimental data, the $R(E)$ line shape was deconvoluted from the $g_{exp}(E)_{OH}$ in order to obtain an instrument independent H-projected density of states for the OH stretching vibrational band. Examples of these $g_{exp}(E)_{OH}$ line shapes for ice, supercooled water, and water are plotted in the upper panel of Figure 7. As a final step of our analysis, the experimental $g_{exp}(E)_H$ derived from Eq. (2) was normalized to 1 in the range 0-500 meV.[46] From $g_{sim}(E)_H$ and $g_{exp}(E)_H$, we derived the corresponding proton mean kinetic energy, $\langle E_K\rangle_{sim}$ and $\langle E_K\rangle_{exp}$,

$$\langle E_K\rangle_{sim(exp)} = \frac{3}{4}\int_0^{480} g_{sim(exp)}(E)_H \coth\frac{\beta E}{2} E dE \qquad (4)$$

with $\beta = 1/(k_B T)$. Furthermore, from $g_{sim}(E)_{OH}$ and $g_{exp}(E)_{OH}$ the mean kinetic energy components for the stretching band, $\langle E_K\rangle_{OH}^{sim}$ and $\langle E_K\rangle_{OH}$, and the effective temperature, $T_{OH}^*$, were obtained,

$$\langle E_K\rangle_{OH}^{sim} = \frac{3}{4}\int_{355}^{500} g_{sim}(E)_{OH} E dE, \qquad (5)$$

$$\langle E_K\rangle_{OH} = \frac{3}{4}\int_{355}^{480} g_{exp}(E)_{OH} E dE = \frac{3\hbar^2}{2M}\sigma_{OH}^2, \qquad (6)$$

$$T_{OH}^* = 2/3k_B\langle E_K\rangle_{OH} = 2/3k_B\langle E_K\rangle_{OH}^{sim}, \qquad (7)$$

where $\sigma_{OH}$ is the standard deviation of the stretching component of the momentum distribution, and in the frequency range of the stretching mode the term $\coth\frac{\beta E}{2}$ is equal to 1. We recall that for T$\rightarrow$ 0 the only contributions to $\langle E_K\rangle_{exp}$ and $\langle E_K\rangle_{OH}$ come from zero point motion. We stress that DINS measures almost directly the kinetic energy of the equilibrium state, i.e., the kinetic energy of ground and excited states for the low energy vibrations (comparable with $k_B$T) and only the ground state for the intramolecular bending and stretching modes of water molecule (because at T $\sim$ 300 K these modes are not excited at all). INS in energy loss configuration measures the transition from the ground state to the first excited state, and in case the system is anharmonic the result in $\langle E_K\rangle_{OH}$ will be in general different compared to the result of $\langle E_K\rangle$ from DINS even at low temperatures. The $\langle E_K\rangle_{OH}$ obtained by INS is based on the framework of a harmonic (normal mode) displacement of the protons in the systems, and, as such, gives access to the effective harmonic component of $\langle E_K\rangle_{OH}$.

The $\langle E_K\rangle_{OH}$ values for ice, water, and supercooled water, calculated from Eq. (6), are plotted as a function of T in the inset of Figure 8. In Table I, $\langle E_K\rangle_{OH}$ and $\langle E_K\rangle_{OH}^{sim}$ values from present INS experiment and density functional theory calculations for ice are reported together with $\langle E_K\rangle$ values from previous DINS experiment[18] and PICPMD simulation.[47] The value of $\langle E_K\rangle$ derived from DINS experiments, $\langle E_K\rangle$ = 156 $\pm$ 2 meV, is larger than that obtained in PICPMD, $\langle E_K\rangle_{sim}$ = 143 $\pm$ 2 meV (see Table I), indicating that these simulations underestimate the proton localization. The error likely stems from the delocalization error of semi-local density functional theory approximations[48] used for the potential energy of the electrons in PICPMD simulations, obtained within approximate DFT. Gradient corrected based functionals, such as PBE and BLYP, tend to yield a slightly weaker covalent bond than in experiments, which in turn lead to a more delocalized motion of the proton. The vdW-DF2 density functional with non-local correlation employed in the present study mitigates the

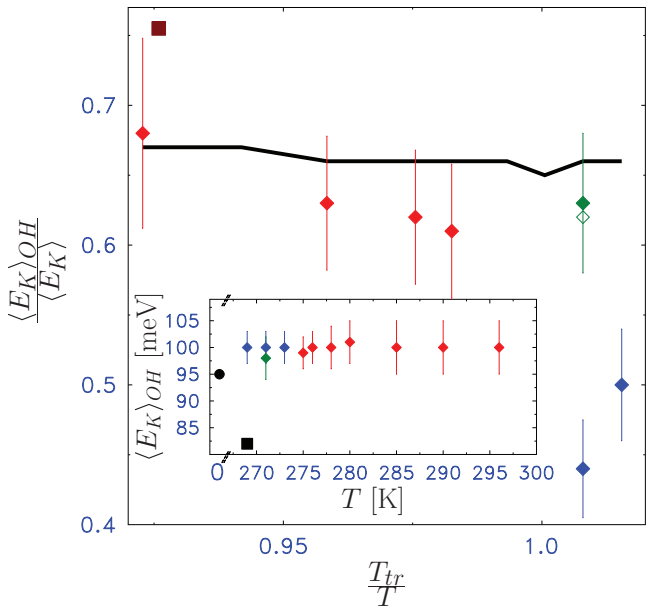


FIG. 8. The ratio of stretching to total kinetic energy as a function of the ratio $\frac{T_{tr}}{T}$, there $T_{tr}$ is the temperature of the triple point (T = 273.16 K). The data are obtained by combining the results from the present experiment with previous DINS measurements carried out at the same temperatures (see Table II for details and references): ice (green diamond), supercooled water (blue diamonds) and stable water, present INS data (red diamonds), and calculated value for vapour phase at T = 295 K, from Ref. 55 ( brown square). The ratio obtained from $\langle E_K\rangle_{exp}$ and $\langle E_K\rangle_{OH}$ from the present INS experiment is reported as a black continuous line for the liquid phase, while the green open diamond is for ice at T = 271 K; the error bars are omitted for clarity and are of similar magnitude as those obtained from the combined INS-DINS data (see Table II for details). (Inset) The $\langle E_K\rangle_{OH}$ values for ice (green diamonds), and stable water (red diamonds) and supercooled water (blue diamonds) as a function of T (see Table II); $\langle E_K\rangle_{OH}^{sim}$ values (from Eq. (5)) from PICPMD[47] results in ice at T = 269 K (black square) and from present DFT results in ice at T = 0 K (black full circle) (see Table I).

problem of the delocalization error (see Table I): the $\langle E_K\rangle_{sim}$ value for ice at T = 0 K, as derived from Eq. (4), is found in remarkable agreement with the experimental value[18] at T = 271 K.

In Table I, we also report the mean kinetic energy for the OH stretching band component, i.e., $\langle E_K\rangle_{OH}^{sim} = 95 \pm 2$, obtained for ice at T = 0, using DFT with the vdW-Df2 functionals (see Eq. (5)). Bearing in mind that thermal contributions to the stretching mean kinetic energy are negligible, i.e., of the order of $10^{-5}$ meV,[6] the agreement between theory and experiments ($\langle E_K\rangle_{OH} = 98 \pm 4$ meV) is satisfactory. For ice at T = 269 K, Table I also reports the calculated value of $\langle E_K\rangle_{OH}^{sim}$ from PICPMD study,[47] obtained using the OH stretching principal frequency $\omega_3$, i.e., $\langle E_K\rangle_{OH}^{sim} = \hbar\omega_3/4 \coth(\hbar\omega_3\beta)$. This value, 85 ± 2 meV, is red-shifted as compared to the value of 98 ± 4 meV obtained from INS experiment, similar to $\langle E_K\rangle_{sim}$ from PICPMD, with respect to $\langle E_K\rangle$ from DINS.

TABLE I. T = 271 K: Values of proton mean kinetic energy, $\langle E_K\rangle_{exp}$ and $\langle E_K\rangle_{OH}$, for ice from the INS measurements carried out in this work, calculated from Eq. (6); $\langle E_K\rangle$ is the value of the proton kinetic energy obtained from previous DINS measurements.[18] T = 269 K: $\langle E_K\rangle_{sim}$ and $\langle E_K\rangle_{OH}^{sim}$ values are from a previous PICPMD study[47] (see text). Theory: $\langle E_K\rangle_{sim}$ and $\langle E_K\rangle_{OH}^{sim}$ values are from the present *ab initio* calculations study; the $\langle E_K\rangle_{com}$ value was obtained from the combination of computed and experimental density of states line shapes at T = 271 K (see Figure 6, top panel).

| T | [K] | Theory | 269 | 271 |
|---|---|---|---|---|
| $\langle E_K\rangle_{exp}$ | [meV] | | | 158 ± 4 |
| $\langle E_K\rangle_{OH}$ | [meV] | | | 98 ± 4 |
| $\langle E_K\rangle_{sim}$ | [meV] | 156 | 143 ± 2 | |
| $\langle E_K\rangle_{OH}^{sim}$ | [meV] | 95 ± 2 | 82 ± 2 | |
| $\langle E_K\rangle_{com}$ | [meV] | 158 ± 2 | | |
| $\langle E_K\rangle$ | [meV] | | | 156 ± 2 |

Values of $\langle E_K\rangle_{OH}$ for all temperatures of the present INS experiment, as derived from Eq. (6), are reported in Table II. The proton mean kinetic energy $\langle E_K\rangle$ from previous DINS measurements,[16] the same quantity derived from the density of states of the present work and the OH stretching to total mean kinetic energy fractions, $\frac{\langle E_K\rangle_{OH}}{\langle E_K\rangle}$, $\frac{\langle E_K\rangle_{OH}}{\langle E_K\rangle}_{exp}$, are also listed in Table II. The $\langle E_K\rangle_{OH}$ as a function of T, the $\frac{\langle E_K\rangle_{OH}}{\langle E_K\rangle}$, $\frac{\langle E_K\rangle_{OH}}{\langle E_K\rangle}_{exp}$, as a function of $\frac{T_{tr}}{T}$, $T_{tr}$ being the temperature of the triple point (T = 273.16 K), are plotted in Figure 8. These quantities provide a direct and quantitative insight into the H-bonding strength in the various phases of water. Indeed, H-bonding affects not only the stretching kinetic energy, but all the kinetic energy components. The ratio of stretching to total kinetic energy shows a peculiar behavior as a function of $\frac{T_{tr}}{T}$: in the vapour phase, the ratio is dominated by the "free" molecule value, with negligible influence from H-bonds; as $\frac{T_{tr}}{T}$ approaches 1, a decrease in the kinetic energy ratio is observed. Such a reduction is interpreted as an indication of an increase of the H-bond strength and/or of anharmonicity in the proton effective potential. We note that the decrease shown by the two determinations, by INS and INS/DINS, of the ratio of stretching to total kinetic energy is quantitatively different, with the latter showing a stronger decrease and with an absolute minimum in the supercooled phase. The ratio $\frac{\langle E_K\rangle_{OH}}{\langle E_K\rangle}_{exp}$, obtained by using INS only, shows a weaker temperature dependence with a relative minimum in the liquid at T = 273 K, and an absolute minimum for ice. As discussed above, these differences arise from the much stronger temperature dependence of the total kinetic energy found in DINS as compared to INS, which is likely to be ascribed to the different sensitivity to ground state details of the two methods.

In the case of ice at T = 0 K, we also derived $g_{com}(E)_H$ (plotted in the top panel of Figure 6). The latter is obtained by combining the H-projected density of states of the OH stretching band, $g_{exp}(E)_{OH}$, with the librational-translational, vibrational, and bending bands components of the simulated $g_{sim}(E)_H$ (plotted as black, solid line in the bottom panel of Figure 6). The corresponding value of $\langle E_K\rangle_{com}$, calculated from

$$\langle E_K\rangle_{com} = \frac{3}{4}\int_0^{480} g_{com}(E)_H \coth\frac{\beta E}{2} E dE \qquad (8)$$

is 158 ± 2 meV (Table III). This result is in excellent agreement with the $\langle E_K\rangle = 156 \pm 2$ meV value from DINS, within the statistical uncertainty. Further, the $\langle E_K\rangle_{exp}$ 158 ± 4 meV value from INS also is in agreement with the DINS value. As a general comment, we note that large systematic uncertainties may be present in the determination of the total kinetic energy from INS, given that the multiple scattering

TABLE II. Values of $\langle E_K\rangle_{OH}$ as a function of temperature (T) derived using Eq. (6). Calculated values for water vapour at T = 295 K are from Ref. 55. Values for ice at T = 269 K are from a previous PICPMD (Path Integral Car-Parrinello Molecular Dynamics) simulation study;[47] values of the total proton mean kinetic energy $\langle E_K\rangle$ are from previous DINS measurements,[16,18] while values of $\langle E_K\rangle_{exp}$ are from the present work: these have been used to estimate the ratios of stretching to total kinetic energy at all temperatures listed in the last two columns.

| Phase | $T$ [K] | $\langle E_K\rangle_{OH}$ [meV] | $\langle E_K\rangle$ [meV] | $\langle E_K\rangle_{exp}$ [meV] | $\frac{\langle E_K\rangle_{OH}}{\langle E_K\rangle}$ | $\frac{\langle E_K\rangle_{OH}}{\langle E_K\rangle_{exp}}$ |
|---|---|---|---|---|---|---|
| Ice** | 269 | 82 | | | | |
| Ice | 271 | 98 ± 4 | 156 ± 2 | 158 ± 4 | 0.63 ± 0.05 | 0.62 ± 0.05 |
| SW | 269 | 100 ± 3 | 199 ± 2 | 152 ± 4 | 0.50 ± 0.04 | 0.66 ± 0.04 |
| SW | 271 | 100 ± 3 | 228 ± 2 | 152 ± 4 | 0.44 ± 0.03 | 0.66 ± 0.03 |
| SW | 273 | 100 ± 3 | | 153 ± 4 | | 0.65 ± 0.04 |
| W | 275 | 99 ± 3 | | 150 ± 3 | | 0.66 ± 0.04 |
| W | 276 | 100 ± 3 | | 152 ± 4 | | 0.66 ± 0.04 |
| W | 278 | 100 ± 4 | 164 ± 1 | 152 ± 4 | 0.61 ± 0.05 | 0.66 ± 0.05 |
| W | 280 | 101 ± 4 | 162 ± 1 | 152 ± 4 | 0.62 ± 0.05 | 0.67 ± 0.05 |
| W | 285 | 100 ± 5 | 160 ± 1 | 151 ± 4 | 0.63 ± 0.05 | 0.66 ± 0.05 |
| W | 290 | 100 ± 5 | | 149 ± 3 | | 0.66 ± 0.05 |
| W | 296 | 100 ± 5 | 146 ± 3 | 150 ± 4 | 0.68 ± 0.07 | 0.67 ± 0.07 |
| Vapour from Ref. 55 | 295 | 115 | 151 | 0.76 | | |

procedure employed is fully reliable only above about 200 meV. This is because the phenomenological approach, i.e., multiple scattering modeled within the IA, applies only above this energy.[37,49]

From $\langle E_K\rangle_{com}$, one can derive the mean kinetic energy component relative to the H internal modes only, i.e., bending (b) and stretching (s). This yields $\langle E_K\rangle_{com}^{b+s} = 121.8$ meV, to be compared with 116.2 meV, calculated in a recent paper[6] within the harmonic approximation, and assuming rotational, translational, and vibrational degrees of freedom are decoupled.

Additional information on the quantum nature of hydrogen in ice and water can be obtained from the study of the hydrogen momentum distribution line shape. We note that, as in the case of $\langle E_K\rangle$, quantum effects on the proton momentum distribution may not be interpreted based on a semiclassical approach. For example, by using a perturbative approach in powers of $\hbar$[50,51] the momentum distribution is approximated as

$$n(p) = \frac{1}{\sqrt{(2M\pi KT^*)^3}} e^{\frac{-p^2}{(2M\pi KT^*)}}, \qquad (9)$$

where $T^* = T + \frac{\hbar^2}{36Mk_B^2T}\langle\nabla^2 V\rangle$, $M$ is the proton mass, and $\langle\nabla^2 V\rangle$ is the average of the Laplacian of the proton potential energy.[51] In the case of ice $I_h$ close to melting ($T = 271$ K), using a quasi-harmonic approximation for $V$, with a single effective angular frequency $\bar{\omega}$ (an average value over stretching, bending, librations, etc.), one obtains $T^* \approx 850$ K, which corresponds to a kinetic energy approximately 30% lower than the experimentally determined value.[18]

In the case of ice, our results from simulations and INS experiments allowed us to reconstruct the hydrogen isotropic harmonic momentum distributions $n_H(p)$ and the OH stretching component of the hydrogen isotropic harmonic momentum distribution $n_{OH}(p)$ variances at T = 0 K, and T = 271 K (from Table III). Likewise, for water at all T, the $n_{OH}(p)$ function, derived using the $\langle E_K\rangle_{OH}$ values in Table II, is a Gaussian line shape with standard deviation equal to $\sigma_{OH}$. The $n_H(p)$ function for ice is plotted in the bottom panel of Figure 5, as a red line. In a recent DINS study of ice at T = 271 K,[18] it was shown that the momentum distribution of each individual proton is well approximated by a multivariate Gaussian distribution, whose three distinct frequencies, $\omega_{1,2,3}$, associated to local principal axes, depend on the crystalline orientation of the molecule to which the proton belongs.[47] This picture corresponds to an anisotropic quasi-harmonic model in which the main effects of anharmonicity are subsumed in the effective frequencies $\omega_i$. From these principal frequencies, one obtains the corresponding principal variances of the momentum distribution: $\frac{\hbar^2\sigma_i^2}{2M} = \frac{\hbar\omega_i}{4}\coth\frac{\beta\hbar\omega_i}{2}; \sigma_i^2 = \frac{M\omega_i}{2\hbar}\coth\frac{\beta\hbar\omega_i}{2}$.

TABLE III. Properties of ice: $\langle E_K\rangle_{OH}$, $\langle E_K\rangle_{com}$ are defined as in Table I; $T^*_{com} = 2/3k_B\langle E_K\rangle_{com}$ and $\sigma_H$ (the average of the principal variances of the momentum distribution line shape, see text), as obtained from best fit of the $n(p)_H$ line shape (see text); the proton mean kinetic energy $\langle E_K\rangle$ is from DINS measurements (Ref. 16) and from previous PICPMD simulation[47] (see text).

| $T$ [K] | $\sigma_H$ [Å$^{-1}$] | $\sigma_{OH}$ [Å$^{-1}$] | $\langle E_K\rangle_{OH}$ [meV] | $T^*_{com}$ [K] | $\langle E_K\rangle_{com}$ [meV] | $\langle E_K\rangle$ [meV] | $\langle E_K\rangle_{sim}$ [meV] |
|---|---|---|---|---|---|---|---|
| 0 | 5.02 | | | 1297 | 158 ± 2 | | 156 |
| 271 | | 3.95 | 98 ± 2 | 757 | | | |
| 271 | 4.99 | | | 1221 | | 156 ± 2 | |
| 269 | | | | 1106 | | | 143 ± 2 |

TABLE IV. Values of principal frequencies $\omega_i$ (see text) and variances $\sigma_i$, principal variances of the momentum distribution line shape, for ice.

| $\omega_i$[meV] | PBE | vdW-DF2 | INS | $\sigma_i$ | [Å$^{-1}$] |
|---|---|---|---|---|---|
| $\omega_1$ | 384 | 404 | 417 | $\sigma_1$ | 7.09 |
| $\omega_2$ | 156 | 150 | 140 | $\sigma_2$ | 4.11 |
| $\omega_3$ | 108 | 95 | 80 | $\sigma_3$ | 3.43 |

Averaging the principal variances $\sigma_i$, we obtain $\sigma_H = 4.99$ Å$^{-1}$, from which we derived the isotropic Gaussian quasi-harmonic component lineshape, $n_H(p)$. The latter, plotted as a blue line in the bottom panel of Figure 5, provides a spherical representation of the anisotropic Gaussian quasi-harmonic DINS line shape (plotted as black dashed line in the bottom panel of Figure 5). We note the remarkable agreement between the isotropic components of both momentum distributions, $n_H(p)$, derived from the present INS study, and the isotropic Gaussian quasi-harmonic component line shape, the $n(p)$, reconstructed from previous and independent DINS experiments.[18]

An analysis of the measured $S(q, \omega)$ intensities of ice in terms of effective frequencies $\omega_i$ yields information about the effects of anharmonicity on the proton potential. In particular, from the INS vibrational spectra of ice at 271 K (see Figure 5), a clear connection emerges between the vibrational spectrum and the main $\omega_i$ frequencies, encompassing: a stretching band $\omega_{str}$ centered at ≈417 meV, a bending band $\omega_{ben}$ centered at ≈200 meV, and a broad libration band $\omega_{lib}$ centered at ≈80 meV. It was shown in Ref. 18 that $\omega_1$, $\omega_3$, and $\omega_2$ consist mainly of weighted averages of stretching, librational, and a mix of bending and librational frequencies, respectively, with red-shifts due to additional network mode contributions and softening caused by anharmonicity.[47] This yields the values of $\omega_1$, $\omega_2 = 1/2(\omega_{ben} + \omega_{lib})$ and $\omega_3$ reported in Table IV. The results obtained for $\omega_i$ from the DFT calculations of the projected DOS using both PBE exchange-correlation functional and vdW-DF2 are also shown for comparison. The three corresponding $\omega_1$, $\omega_2$, and $\omega_3$ were derived for ice, and an anisotropic spherically averaged $n_H(p)$ was obtained, which includes the effects of anharmonicity. This function and the one independently derived from previous DINS experiments[18] are in perfect agreement (see top panel of Figure 5).

## IV. SUMMARY AND CONCLUSIONS

In summary, INS experimental data supported by *ab initio* simulations were used to unambiguously derive the harmonic and anharmonic zero-point components of $n_H(p)$ in ice, and the $n_{OH}(p)$ function line shape in ice, water, and supercooled water. Moreover, our results, in conjunction with the parametric fitting analysis currently employed to analyze DINS data, provided additional and independent information. In the case of ice, we found that the anharmonic momentum distribution components derived from INS are in remarkable agreement, within the experimental uncertainty, with those from previous and independent DINS experiments,[18] indicating that the proton dynamics is well described within a quasi-harmonic approximation. We quantified the OH stretching contribution to $n_H(p)$ in ice, water at ambient conditions and supercooled water, and we discussed its role in determining the tail behavior of the momentum distribution line shape. We found that the zero-point stretching vibration energy is very similar in supercooled and stable water. Since the OH stretching contributions to the total $n_H(p)$ line shapes[16] are almost constant for liquid water at all T, an additional mechanism has to be invoked to fully account for the high momentum tails observed in supercooled water[16] which show the signature of a secondary shoulder at high momenta, both in light[12] and heavy water.[52] We stress that such secondary shoulders are not found in water at ambient conditions.[4] On the contrary, the tail of the $n_H(p)$ in ice are in remarkably good agreement with $n(p)$ resulting from DINS experiments[18] (see Figure 9). Present INS results provided an estimate of three distinct frequencies, $\omega_{1,2,3}$, associated to local principal axes of the multivariate Gaussian distribution. The principal frequencies extracted from *ab initio* simulations, using non-local van der Waals functionals for water and ice, are in good

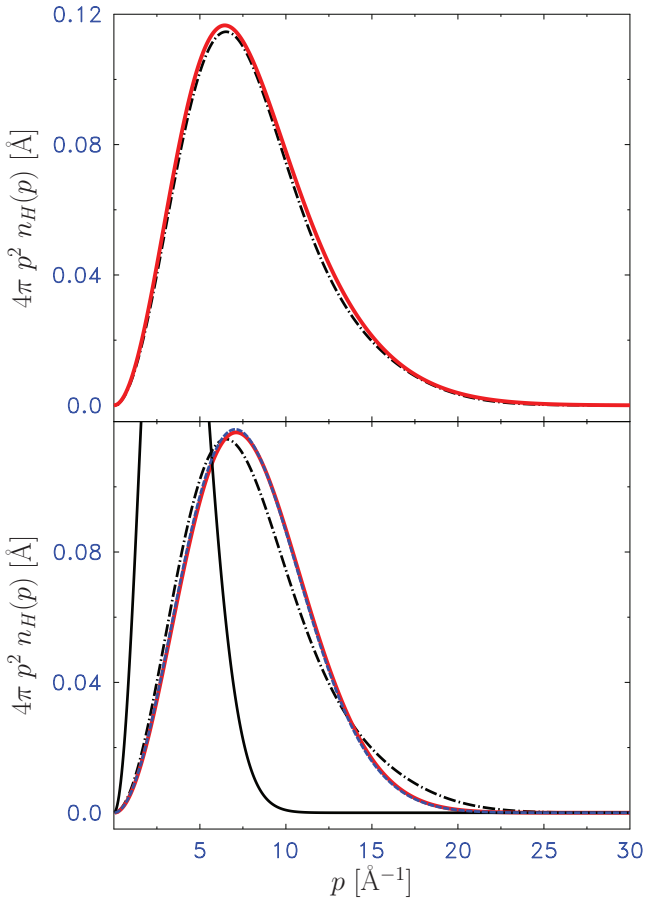


FIG. 9. (Top panel) The radial, spherically averaged, anisotropic proton momentum distribution for polycrystalline ice at T = 271 K, derived from the present study (red line) and from DINS experiment (black dashed-dotted line).[18] (Bottom panel) The classical Maxwell distribution for a proton at T = 271 K (solid black line); the isotropic harmonic component of the radial proton momentum distribution, derived from $g_{com}(E)_H$ (see text and Eq. (8)) with $\sigma_H = 5.02$ Å$^{-1}$, T* = 1297 K) (red line); the isotropic gaussian quasi-harmonic component (blue line) with $\sigma_H = 4.99$ Å$^{-1}$ and T* = 1221 K, derived from DINS experiments,[18] and the spherically averaged, anisotropic proton momentum from DINS,[18] plotted as black dashed-dotted line.

agreement with those derived from the INS experiment (see Table IV).

Furthermore new, additional insight on the quantum effects on the OH stretching frequency was provided through the derivation, for the first time, of the mean kinetic energy values associated with the OH stretching vibrational mode, $\langle E_K \rangle_{OH}$. Our results showed that $\langle E_K \rangle_{OH}$ is nearly constant as a function of T, indicating that quantum effects on the OH stretching frequency depend weakly on T. The ratio $\frac{\langle E_K \rangle_{OH}}{\langle E_K \rangle}$ provides a measure of the H-bond strength as a function of T: it increases towards the vapour phase, i.e., H-bonding weakens; it reduces in the stable liquid and ice, as proton covalent bond softens, i.e., H-bonding is strengthened. We stress that this behavior is in agreement with previous theoretical estimates, which predict that the contribution of kinetic energy from intramolecular vibrations to the total kinetic energy decreases from the isolated molecules (i.e., vapour), to liquid water and then ice.[53] Our work however shows that the minimum values of the $\frac{\langle E_K \rangle_{OH}}{\langle E_K \rangle}$ ratio are attained in supercooled water; this finding, in combination with the structural modifications of the first and second coordination shell found in diffraction measurements,[33] supports a picture where intermolecular interactions are stronger in metastable phases of water than in ice, in contrast to the commonly accepted picture of weaker H-bonds in supercooled water than in ice.

Our findings on supercooled water represent an exception to the correlation suggested by Li *et al.*,[31] i.e., the present results for supercooled water differ from those suggested by Li *et al.*[31] for water at ambient conditions, as far as quantum effects on intramolecular stretching and intermolecular bending modes are concerned. Indeed, the present measurements show that both stretching and intramolecular bending frequencies vary weakly with T, the larger variation being observed in the case of ice. These findings shed some light on the physical origin of the excess in mean kinetic energy measured by DINS experiments in supercooled water.[16] The percentage contribution of $\langle E_K \rangle_{OH}$ to $\langle E_K \rangle_H$ in supercooled water is smaller than in water at ambient conditions. The delicate interplay between internal and external contributions to the total zero point energy are not immediately captured by DINS or INS alone. On one hand, the kinetic energy ratio obtained by INS alone, besides being subject to larger systematic uncertainties and based on the assumption of harmonic dynamics, shows a slight decrease from the liquid to the solid phase, with a minimum in polycrystalline ice. The static structural information from neutron and X-ray diffraction, on the other hand, shows a remarkable contraction of the first and second neighbour O–O correlation distances in the supercooled liquid, which would be expected to have a more marked influence on the vibrational spectrum than the measured shifts in the OH stretching between ambient, supercooled, and ice phases. The ratio obtained from the combination of INS/DINS is dominated by the large excess of the total kinetic energy found in the supercooled phases by DINS, with a minimum in the supercooled phase. The discrepancies may reside in correlated proton motions in presence of various degrees of anharmonicity, in the interpretation described in Ref. 54 for high pressure ice. Such effects have not been predicted by theory but may be present in the supercooled phase, giving rise to the peculiar momentum distributions found by DINS measurements in both light and heavy water.

Finally, we note that the principal frequencies computed via vdw-DF2 provided a better representation of both the strength of covalent bonds (too soft in PBE) and of the H-bonds (too strong in PBE) than GGA based functionals. However, it remains to be seen if the better agreement with experiments persist when the vdW-DF2 potential energy surface is used in conjunction with PICPMD calculations.

Overall, the present study on the microscopic quantum dynamics of water and ice strongly suggests that the generally accepted picture of relatively weak H-bonds in supercooled water, in the presence of tunneling or anharmonic potentials, may need to be reconsidered. The large difference between the momentum distributions of normal and supercooled water may stem from correlated proton motion in the ground state of supercooled water with an associated quantum coherence length, due to the simultaneous presence of O–O shortening and H-bond bendings.

## ACKNOWLEDGMENTS

This work was supported within the CNR-STFC Agreement No. 06/20018 concerning collaboration in scientific research at the spallation neutron source ISIS. The work was supported by the Consiglio Nazionale delle Ricerche and by META project – Materials Enhancement for Technological Applications – FP7-PEOPLE-2010-IRSES. The work at Spallation Neutron Source was supported by the Scientific User Facility Division, Office of Basic Energy Sciences, (U.S.) Department of Energy (DOE). ORNL is managed by UT-Battelle, LLC under contract DE-AC0500OR22725 for the (U.S.) Department of Energy. E.M. and G.G. gratefully acknowledge DOE-CMSN, under Grant No. DE-SC0005180.

[1] T. D. Kühne and R. Z. Khaliullin, Nat. Commun. **4**, 1450 (2013).
[2] M. Bellissent-Funel, *Hydration Processes in Biology: Theoretical and Experimental Approaches*, Vol. 305 of NATO Science Series: Life Sciences (IOS Press, 1999).
[3] P. G. Debenedetti, *Metastable Liquids: Concepts and Principles*, Physical Chemistry (Princeton University Press, 1996).
[4] C. Andreani, D. Colognesi, A. Pietropaolo, and R. Senesi, Chem. Phys. Lett. **518**, 1 (2011).
[5] M. Ceriotti and D. E. Manolopoulos, Phys. Rev. Lett. **109**, 100604 (2012).
[6] R. Moreh and D. Nemirovsky, J. Chem. Phys. **133**, 084506 (2010).
[7] G. Reiter and R. Silver, Phys. Rev. Lett. **54**, 1047 (1985).
[8] G. F. Reiter, J. Mayers, and J. Noreland, Phys. Rev. B **65**, 104305 (2002).
[9] G. F. Reiter, J. Mayers, and P. Platzman, Phys. Rev. Lett. **89**, 135505 (2002); e-print arXiv:cond-mat/0203108.
[10] C. Andreani, D. Colognesi, J. Mayers, G. F. Reiter, and R. Senesi, Adv. Phys. **54**, 377 (2005).
[11] C. Andreani, D. Colognesi, E. Degiorgi, and M. A. Ricci, J. Chem. Phys. **115**, 11243 (2001).
[12] A. Pietropaolo, R. Senesi, C. Andreani, A. Botti, M. A. Ricci, and F. Bruni, Phys. Rev. Lett. **100**, 127802 (2008).
[13] J. M. F. Gunn, C. Andreani, and J. Mayers, J. Phys. C **19**, L835 (1986).
[14] R. Senesi, C. Andreani, Z. Bowden, D. Colognesi, E. Degiorgi, A. L. Fielding, J. Mayers, M. Nardone, J. Norris, M. Praitano *et al.*, Physica B **276**, 200 (2000).
[15] A. Pietropaolo and R. Senesi, Phys. Rep. **508**, 45 (2011).
[16] A. Pietropaolo, R. Senesi, C. Andreani, and J. Mayers, Braz. J. Phys. **39**, 318 (2009).
[17] A. Pietropaolo, R. Senesi, C. Andreani, A. Botti, M. A. Ricci, and F. Bruni, Phys. Rev. Lett. **103**, 069802 (2009).

[18]D. Flammini, A. Pietropaolo, R. Senesi, C. Andreani, F. McBride, A. Hodgson, M. A. Adams, L. Lin, and R. Car, J. Chem. Phys. **136**, 024504 (2012).
[19]C. Pantalei, A. Pietropaolo, R. Senesi, S. Imberti, C. Andreani, J. Mayers, C. Burnham, and G. Reiter, Phys. Rev. Lett. **100**, 177801 (2008).
[20]C. J. Burnham, G. F. Reiter, J. Mayers, T. Abdul-Redah, H. Reichert, and H. Dosch, Phys. Chem. Chem. Phys. **8**, 3966 (2006).
[21]J. A. Morrone and R. Car, Phys. Rev. Lett. **101**, 017801 (2008).
[22]J. A. Morrone, L. Lin, and R. Car, J. Chem. Phys. **130**, 204511 (2009).
[23]C. J. Burnham, T. Hayashi, R. L. Napoleon, T. Keyes, S. Mukamel, and G. F. Reiter, J. Chem. Phys. **135**, 144502 (2011).
[24]É. D. Murray and G. Galli, Phys. Rev. Lett. **108**, 105502 (2012).
[25]C. Zhang, J. Wu, G. Galli, and F. Gygi, J. Chem. Theory Comput. **7**, 3054 (2011).
[26]J. A. Morrone, V. Srinivasan, D. Sebastiani, and R. Car, J. Chem. Phys. **126**, 234504 (2007).
[27]F. Perakis and P. Hamm, J. Phys. Chem. B **115**, 5289 (2011).
[28]M. A. Ricci, M. Nardone, A. Fontana, C. Andreani, and W. Hahn, J. Chem. Phys. **108**, 450 (1998).
[29]C. Andreani, P. Bosi, F. Sacchetti, and C. K. Loong, J. Chem. Phys. **83**, 750 (1985).
[30]K. Toukan, M. A. Ricci, S.-H. Chen, C.-K. Loong, D. L. Price, and J. Teixeira, Phys. Rev. A **37**, 2580 (1988).
[31]X.-Z. Li, B. Walker, and A. Michaelides, Proc. Natl. Acad. Sci. U.S.A. **108**, 6369 (2011).
[32]A. Botti, F. Bruni, A. Isopo, M. A. Ricci, and A. K. Soper, J. Chem. Phys. **117**, 6196 (2002).
[33]M. A. Ricci, F. Bruni, and A. Giuliani, Faraday Discuss. **141**, 347 (2009).
[34]A. Soper, Chem. Phys. **258**, 121 (2000).
[35]J.-L. Kuo, M. L. Klein, and W. F. Kuhs, J. Chem. Phys. **123**, 134505 (2005).
[36]U. Bergmann, A. D. Cicco, P. Wernet, E. Principi, P. Glatzel, and A. Nilsson, J. Chem. Phys. **127**, 174504 (2007).
[37]C. Andreani, V. Merlo, and M. A. Ricci, Nucl. Instrum. Methods Phys. Res. B **36**, 216 (1989).
[38]C. Andreani, V. Merlo, M. A. Ricci, and B. C. Boland, Mol. Phys. **66**, 747 (1989).
[39]P. Giannozzi, S. Baroni, N. Bonini, M. Calandra, R. Car, C. Cavazzoni, D. Ceresoli, G. L. Chiarotti, M. Cococcioni, I. Dabo *et al.*, J. Phys. Condens. Matter **21**, 395502 (2009).
[40]K. Lee, É. D. Murray, L. Kong, B. I. Lundqvist, and D. C. Langreth, Phys. Rev. B **82**, 081101(R) (2010).
[41]A. I. Kolesnikov, J.-M. Zanotti, C.-K. Loong, P. Thiyagarajan, A. P. Moravsky, R. O. Loutfy, and C. J. Burnham, Phys. Rev. Lett. **93**, 035503 (2004).
[42]G. E. Granroth, A. I. Kolesnikov, T. E. Sherline, J. P. Clancy, K. A. Ross, J. P. C. Ruff, B. D. Gaulin, and S. E. Nagler, J. Phys.: Conf. Ser. **251**, 012058 (2010).
[43]J. Li and A. Kolesnikov, J. Mol. Liq. **100**, 1 (2002).
[44]V. Sears, Adv. Phys. **24**, 1 (1975).
[45]D. Vanderbilt, Phys. Rev. B **32**, 8412 (1985).
[46]C. Andreani, J. Mayers, P. Postorino, and M. A. Ricci, Mol. Phys. **73**, 737 (1991).
[47]L. Lin, J. A. Morrone, R. Car, and M. Parrinello, Phys. Rev. B **83**, 220302(R) (2011).
[48]A. J. Cohen, P. Mori-Snchez, and W. Yang, Science **321**, 792 (2008).
[49]C. Andreani, V. Merlo, P. Postorino, and M. Ricci, J. Mol. Struct. **250**, 385 (1991).
[50]E. Wigner, Phys. Rev. **40**, 749 (1932).
[51]W. C. Kerr and K. S. Singwi, Phys. Rev. A **7**, 1043 (1973).
[52]A. Giuliani, F. Bruni, M. A. Ricci, and M. A. Adams, Phys. Rev. Lett. **106**, 255502 (2011).
[53]R. Ramírez and C. P. Herrero, Phys. Rev. B **84**, 064130 (2011).
[54]L. Lin, J. Morrone, and R. Car, J. Stat. Phys. **145**, 365 (2011).
[55]M. Vos, E. Weigold, and R. Moreh, J. Chem. Phys. **138**, 044307 (2013).